

25.1% High-Efficiency Monolithic Perovskite Silicon Tandem Solar Cell with a High Bandgap Perovskite Absorber

Patricia S. C. Schulze,* Alexander J. Bett, Martin Bivour, Pietro Caprioglio, Fabian M. Gerspacher, Özde Ş. Kabaklı, Armin Richter, Martin Stolterfoht, Qinxin Zhang, Dieter Neher, Martin Hermle, Harald Hillebrecht, Stefan W. Glunz, and Jan Christoph Goldschmidt

Monolithic perovskite silicon tandem solar cells can overcome the theoretical efficiency limit of silicon solar cells. This requires an optimum bandgap, high quantum efficiency, and high stability of the perovskite. Herein, a silicon heterojunction bottom cell is combined with a perovskite top cell, with an optimum bandgap of 1.68 eV in planar p–i–n tandem configuration. A methylammonium-free $\text{FA}_{0.75}\text{Cs}_{0.25}\text{Pb}(\text{I}_{0.8}\text{Br}_{0.2})_3$ perovskite with high Cs content is investigated for improved stability. A 10% molarity increase to 1.1 M of the perovskite precursor solution results in ≈ 75 nm thicker absorber layers and 0.7 mA cm^{-2} higher short-circuit current density. With the optimized absorber, tandem devices reach a high fill factor of 80% and up to 25.1% certified efficiency. The unencapsulated tandem device shows an efficiency improvement of 2.3% (absolute) over 5 months, showing the robustness of the absorber against degradation. Moreover, a photoluminescence quantum yield analysis reveals that with adapted charge transport materials and surface passivation, along with improved antireflection measures, the high bandgap perovskite absorber has the potential for 30% tandem efficiency in the near future.

recombination into consideration, the maximum efficiency of a silicon solar cell is 29.4%.^[2] To exceed this single-junction limit, an absorber with higher bandgap can be stacked on top in a tandem configuration to reduce thermalization losses. The optimal top cell bandgap is 1.72 eV, pushing the Shockley–Queisser limit to 42–44% for a silicon-based tandem solar cell.^[3,4] Simulation under real-world conditions predicts 32–38% with an optimized perovskite bandgap of 1.65–1.74 eV.^[5,6] First tandem devices were realized using MAPbI_3 (MA for methylammonium $(\text{CH}_3\text{NH}_3)^+$) with a too low bandgap of 1.6 eV reaching 13.7% efficiency.^[7] Since then, an enormous rise in efficiency has been achieved by switching to more advanced mixed-cation lead mixed-halide compositions with higher bandgap and changing the device polarity to p–i–n with optically more suitable charge transport materials. The first of these

p–i–n tandem devices was reported by Bush et al. with a 1.64 eV $\text{FA}_{0.83}\text{Cs}_{0.17}\text{Pb}(\text{I}_{0.83}\text{Br}_{0.17})_3$ absorber (FA for formamidinium $[\text{HC}(\text{NH}_2)_2]^+$) and a certified efficiency of 23.6%.^[8] Within the group of $\text{FA}_{1-x}\text{Cs}_x\text{Pb}(\text{I}_{1-y}\text{Br}_y)_3$, fully textured devices with improved light management were realized with a lower bandgap of around 1.6 eV increasing certified efficiency to 25.2%.^[9,10]

1. Introduction

Perovskite silicon tandem solar cells are promising candidates to overcome the theoretical limit of silicon solar cells that so far dominate the photovoltaic market. The Shockley–Queisser limit for a 1.12 eV bandgap absorber is $\approx 33\%$ ^[1]—taking Auger


P. S. C. Schulze, A. J. Bett, Dr. M. Bivour, F. M. Gerspacher, Ö. Ş. Kabaklı, Dr. A. Richter, Q. Zhang, Dr. M. Hermle, Prof. S. W. Glunz, Dr. J. C. Goldschmidt
Division Photovoltaics
Fraunhofer Institute for Solar Energy Systems
Heidenhofstraße 2, 79110 Freiburg, Germany
E-mail: patricia.schulze@ise.fraunhofer.de

P. S. C. Schulze, Prof. H. Hillebrecht
Institute of Inorganic and Analytical Chemistry
University of Freiburg
79104 Freiburg, Germany

P. Caprioglio, Dr. M. Stolterfoht, Prof. D. Neher
Institute of Physics and Astronomy
University of Potsdam
14476 Potsdam, Germany

P. Caprioglio
Young Investigator Group Perovskite Tandem Solar Cells
Helmholtz-Zentrum Berlin für Materialien und Energie GmbH
Kekuléstraße 5, Berlin 12489, Germany

Prof. S. W. Glunz
Laboratory for Photovoltaic Energy Conversion, Department for Sustainable Systems Engineering (INATECH)
University of Freiburg
79110 Freiburg, Germany

 The ORCID identification number(s) for the author(s) of this article can be found under <https://doi.org/10.1002/solr.202000152>.

© 2020 The Authors. Published by WILEY-VCH Verlag GmbH & Co. KGaA, Weinheim. This is an open access article under the terms of the Creative Commons Attribution-NonCommercial-NoDerivs License, which permits use and distribution in any medium, provided the original work is properly cited, the use is non-commercial and no modifications or adaptations are made.

DOI: 10.1002/solr.202000152

Other groups published triple cation compositions (FA–MA–Cs) with bandgaps ranging from 1.59 to 1.64 eV and certified efficiencies up to 25.2%.^[11–14] The company Oxford PV surpassed the record for single-junction silicon solar cell with 28% certified efficiency; however, details on the device stack or processing conditions were not provided.^[15] Very recently, Helmholtz Center Berlin announced a new certified record of 29.15%; so far, details on the processing or the absorber are not available.^[16] Monolithic perovskite silicon tandem solar cells with an optimum bandgap of 1.65–1.7 eV have been reported with up to 27% efficiency, however, without providing certification.^[12,17–22] Very recently (around the start of the submission process of this article), a 25.8% certification for a 1.67 eV was reported by Xu et al. achieving also excellent efficiency in semitransparent solar cells with a one-step gas-assisted perovskite processing method and the addition of chlorine.^[22]

In this work, we apply perovskite absorbers with optimum optical bandgap of 1.68 eV for the highest Si-based tandem efficiency potential. The absorber thickness is adjusted by the perovskite precursor’s molarity for increased absorption. To guarantee good device stability, we focus on MA-free and Cs-rich FA_{0.75}Cs_{0.25}Pb(I_{0.8}Br_{0.2})₃ perovskite compositions for improved thermal and photostability, respectively.^[21–24] Indeed, good stability under working conditions and an efficiency improvement over several months are observed for tandem devices when stored in the dark under N₂. A highest certified efficiency of 25.1% is achieved with our adapted 1.68 eV perovskite absorber layer. Finally, we show that the potential of the high bandgap absorbers is not yet fully exploited and that unsuited charge transport layers and reflection losses are currently limiting the overall tandem performance.

2. Results

2.1. Fabrication

The realized tandem solar cells consist of a planar p–i–n perovskite solar cell on top of a rear-side textured heterojunction silicon solar cell (Figure 1a). The bottom solar cell features phosphorous and boron-doped amorphous silicon (a-Si) as selective contacts and intrinsic a-Si as passivation layers. The bottom cell is connected in series with the top cell via an indium tin oxide (ITO) recombination layer. The perovskite top cell is fabricated via low-temperature processes only ($\leq 100^\circ\text{C}$) to avoid any degradation of the bottom cell. First, the hole transport layer poly[bis(4-phenyl)(2,4,6-trimethylphenyl)amine] (PTAA) is spin coated. On top, poly(9,9-bis(3’-(*N,N*-dimethyl)-*N*-ethylammonium-propyl-2,7-fluorene)-alt-2,7-(9,9-dioctylfluorene))dibromide (PFN-Br) is used as wetting agent for the subsequent perovskite spin coating.^[25] Here, the perovskite composition FA_{0.75}Cs_{0.25}Pb(I_{0.8}Br_{0.2})₃ is used. Evaporated C₆₀ serves as the electron contact. A not fully stoichiometric tin dioxide (SnO_x) buffer layer is deposited with atomic layer deposition (ALD) to avoid sputter damage in the following ITO sputter process for the semitransparent front electrode. Both ITO layers (interconnection and front side contact) are sputtered through a mask with four openings of 6 mm × 6 mm defining four individual solar cells per substrate (photograph in Figure 1b). Ag electrodes were evaporated through a mask defining a U-shaped busbar for each of the four ITO pads and contact pads for external electrical connection of the solar cells (Figure 1b). Finally, evaporated MgF₂ is applied to reduce front side reflection. For current–voltage (*I*–*V*) measurements, a shadow mask with an opening of 5 mm × 5 mm

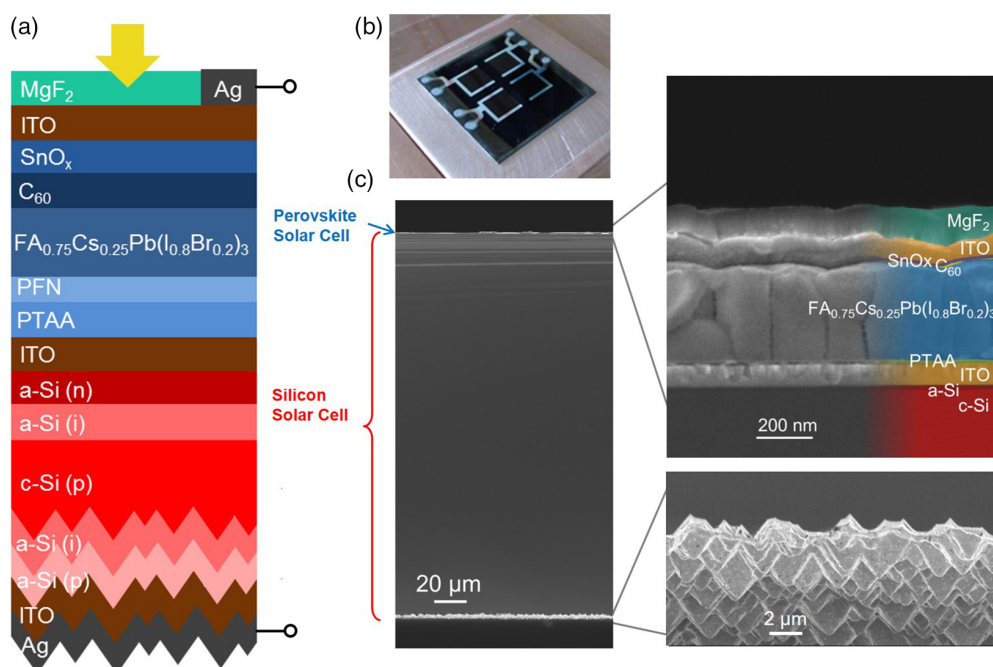


Figure 1. a) Schematic structure of monolithic perovskite silicon tandem solar cells combining a high bandgap perovskite top cell with a silicon heterojunction bottom cell. b) Photograph of a tandem substrate with four active cell areas. c) SEM image (cross section) of a tandem device with zooms of the perovskite top cell and the silicon rear-side texture, respectively.

is used to define the active cell area. The scanning electron microscope (SEM) cross section of a tandem solar cell (Figure 1c) illustrates the difference in size of the two subcells ($\approx 250 \mu\text{m}$ -thick silicon wafer and $< 1 \mu\text{m}$ -thick perovskite solar cell). Zooming into the top cell shows a pinhole free absorber with large crystal grains and thin charge transport layers.

2.2. Optimization of the Top Cell's High Bandgap Perovskite Absorber

2.2.1. Bandgap Tuning and Molarity Adaption

MA-free mixed-cation mixed-halide perovskites like $\text{FA}_{1-x}\text{Cs}_x\text{Pb}(\text{I}_{1-y}\text{Br}_y)_3$ are suitable for top cell absorbers in tandem applications. Here, a low bandgap composition $\text{FA}_{0.83}\text{Cs}_{0.17}\text{Pb}(\text{I}_{0.83}\text{Br}_{0.17})_3$ with an optical bandgap of 1.63–1.64 eV as obtained from Tauc plots and a high bandgap composition $\text{FA}_{0.75}\text{Cs}_{0.25}\text{Pb}(\text{I}_{0.8}\text{Br}_{0.2})_3$ with an optical bandgap of 1.68–1.70 eV are investigated.^[8,18,21] The high bandgap absorber was chosen after compositional engineering with adjustment of the Cs–Br ratio for improved photostability.^[21] Bandgap tuning toward higher energies implies a reduction of short-circuit current density (J_{SC}); therefore, increasing the thickness of the absorber layer is an important challenge. **Figure 2** shows the effect of molarity increase in the perovskite precursor solution on the photovoltaic performance parameters, the absorptance, and external quantum efficiency (EQE) in single-junction perovskite solar cells. Twelve solar cells per group were produced; defective or interrupted I - V curves were not taken into consideration. Average photovoltaic parameters are shown in Table S1, Supporting Information.

The I - V results show that molarity optimization increased the average current generation of the high bandgap absorber ($\text{FA}_{0.75}\text{Cs}_{0.25}\text{Pb}(\text{I}_{0.8}\text{Br}_{0.2})_3$) from 17.5 mA cm^{-2} (1.0 M) to 18.4 mA cm^{-2} (1.1 M) closer to the 18.9 mA cm^{-2} of the reference cell with a lower bandgap (1.0 M $\text{FA}_{0.83}\text{Cs}_{0.17}\text{Pb}(\text{I}_{0.83}\text{Br}_{0.17})_3$), which can be attributed to the improved absorptance from 600 nm to the absorber's band edge as shown in EQE and absorptance measurements (Figure 2d,e). Moreover, the open-circuit voltage (V_{OC}) and especially the fill factor (FF) improved significantly for increased molarity (see Table S1, Supporting Information). The expected V_{OC} advantage of the higher bandgap absorber only occurs for 1.1 and 1.2 M compositions, whereas the highest FF (up to 77%) is obtained for cells with the 1.1 M high bandgap absorber. Thus, fine-tuning of the molarity to 1.1 M allows pushing the overall efficiency up to 15%, similar to our 1.0 M low bandgap reference, and shows reduced data spread. Possible reasons for the strong impact of molarity variation on all photovoltaic parameters are discussed in Section 2.2.2. We also note that bandgap determination via x -axis intercept of a linear fit of the EQE and the absorption onset, respectively, gives different values of 1.64 and 1.68 eV for the high bandgap absorber and 1.61 and 1.64 eV for the low bandgap absorber with a discrepancy of 30–40 meV. In fact, it has been noted before that the effective bandgap of a solar cells is better approximated by taking the peak of the derivative of the EQE, which matches the values obtained from the Tauc plots.^[26,27]

2.2.2. Perovskite Thickness and Wrinkling

SEM analysis of cell cross sections confirms the targeted increase in average film thickness with increasing precursor molarity

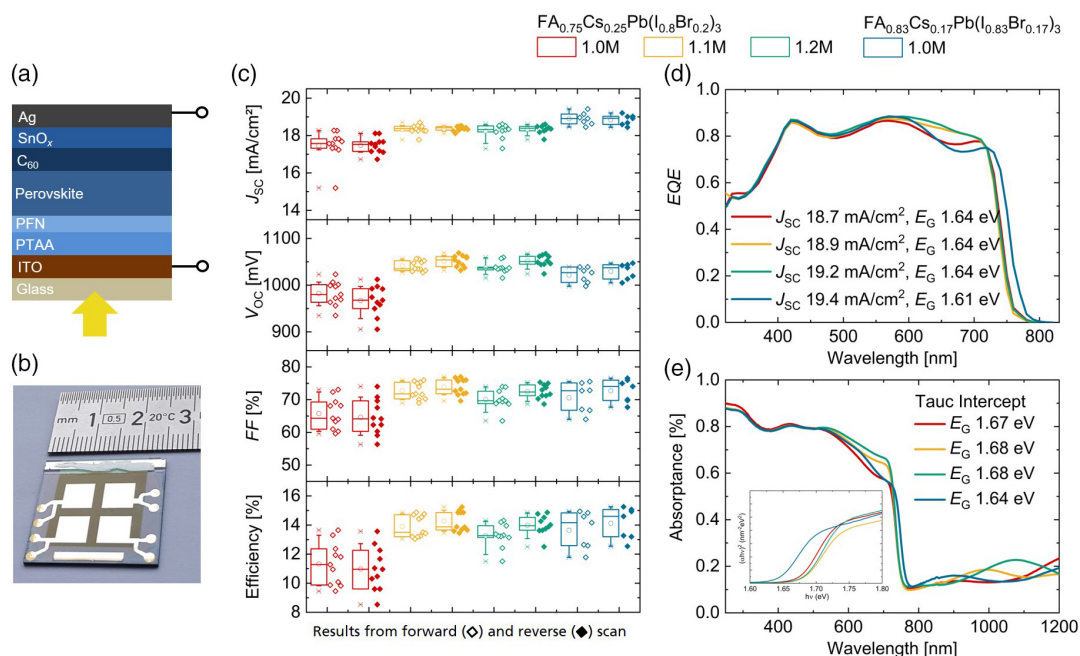


Figure 2. a) Schematic structure of an opaque single-junction solar cell. b) Photograph of a glass substrate with four active cell areas. c) Photovoltaic parameters of perovskite single-junction solar cells with variation in the precursor's molarity and composition. d) EQE measurements with integrated J_{SC} and determined bandgap (from intercept) for each group tested. e) Absorptance and Tauc plot (inset) with optical bandgap determination (from intercept) for each molarity or composition. Improved absorption and current collection are achieved with increased precursor molarity.

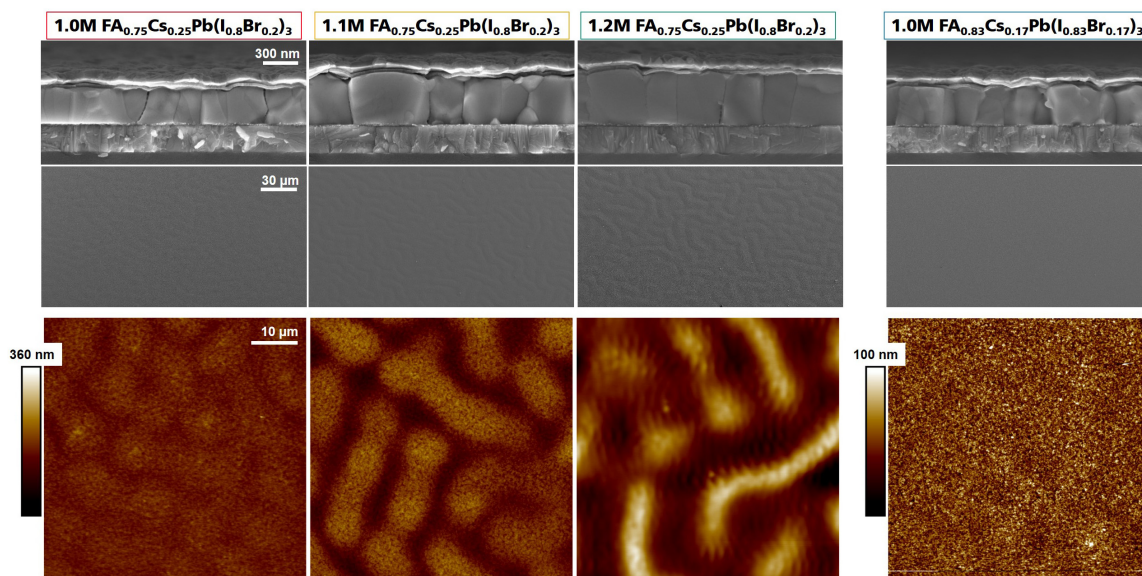


Figure 3. SEM images of single-junction perovskite solar cells (cross section) and PTAA/PFN/perovskite samples (top view), as well as AFM images. The perovskite's layer thickness, quality, and roughness are strongly influenced by molarity and composition.

(Figure 3). However, we note that within the range tested, the relation is not linear; a clear average film thickness increase of +24% (+76 nm) is present from 1.0 to 1.1 M, whereas a fairly small increase of +3% (+10 nm) takes place from 1.1 to 1.2 M (Table 1). These results match well with the respective J_{SC} values presented in section 2.2.1. Consistent with the $I-V$ results, the best perovskite layer quality with large crystal grains was obtained for 1.1 M. Additional SEM top-view images with high magnification (Figure S1, Supporting Information) show pinhole-free films for all compositions and suggest the largest average grain size for the 1.1 M high bandgap precursor solution and the smallest average grain size for the 1.0 M low bandgap precursor solution. Moreover, the change in the precursor's molarity also affects the surface texture on a larger scale. SEM top-view images with low magnification of the respective perovskite layers reveal that the surface is changing from rather flat to a wrinkled structure. Atomic force microscopy (AFM) analysis supports this observation, quantified by an increase in surface roughness (average roughness R_a and root mean square roughness R_q ; Table 1). Along with an increased film roughness, the standard deviation of the film thickness is affected.

Our observations align with the existing literature describing compositional or thickness changes to affect the perovskite's morphology.^[28–30] Here, in-plane compressive stress in the intermediate phase of film formation, triggered by a substrate with a lower coefficient of thermal expansion, and consequent energy release resulting in a wrinkled morphology are identified as an underlying mechanism.^[30] All results from our application-relevant molarity variation suggest that the precursor solution's molarity has strong influence on the crystallization dynamics and, thus, film roughness and wrinkling, but does not show a linear relation to average film thickness (Figure S2, Supporting Information). Moreover, a reduced absorbance around the band edge is present for the 1.0 M perovskite absorbers, primarily due to their reduced layer thickness and possibly due to a higher degree of structural and/or stoichiometric disorder in the film due to small grain formation. A 10% increase in molarity to 1.1 M not only leads to a significant increase in layer thickness but also impacts the whole crystallization dynamics and grain growth resulting in films with large crystal grains and probably less defects, with positive effect on all solar cell parameters. Braunger et al. reported J_{SC} and especially V_{OC}

Table 1. Perovskite layer evolution regarding thickness and surface wrinkling dependent on the precursor solution's molarity and composition. R_a and R_q stand for average and root mean square roughness, respectively.

Perovskite precursor solution	Perovskite layer thickness ^{a)} [nm]	Perovskite surface texture ^{b)}	Perovskite surface roughness ^{c)}	
			R_a [μ m]	R_q [μ m]
1.0 M $FA_{0.75}Cs_{0.25}Pb(I_{0.8}Br_{0.2})_3$	324 ± 12	Rather flat	0.011	0.013
1.1 M $FA_{0.75}Cs_{0.25}Pb(I_{0.8}Br_{0.2})_3$	400 ± 27 (+24%) ^{d)}	Emerging wrinkles	0.026	0.032
1.2 M $FA_{0.75}Cs_{0.25}Pb(I_{0.8}Br_{0.2})_3$	410 ± 45 (+27%) ^{d)}	Wrinkled	0.042	0.053
1.0 M $FA_{0.83}Cs_{0.17}Pb(I_{0.83}Br_{0.17})_3$	336 ± 14 (+4%) ^{d)}	Flat	0.011	0.014

^{a)}Estimated from SEM cross-sectional analysis at four positions with mean value and standard deviation; ^{b)}From SEM top-view images; ^{c)}From AFM analysis; ^{d)}Change in percentage compared with layer thickness of 1.0 M $FA_{0.75}Cs_{0.25}Pb(I_{0.8}Br_{0.2})_3$.

improvement comparing flat and moderately wrinkled low bandgap $\text{FA}_{0.83}\text{Cs}_{0.17}\text{Pb}(\text{I}_{0.83}\text{Br}_{0.17})_3$ in p-i-n perovskite solar cells and assumed the larger grain size and strain effects to cause the higher V_{OC} of wrinkled films.^[28] In our case, a further increase in molarity to 1.2 M led to pronounced wrinkling, but did not seem to improve the film quality any further. So far, we did not observe a negative effect of wrinkles on the device performance; however, strain-related long-term effects on device performance and stability should be addressed in future studies. Moreover, wrinkled surfaces set high requirements for subsequent thin film depositions. Here, vacuum-based processes like evaporation, ALD, and sputtering, or spray coating are suitable techniques. In our case, 15 nm of evaporated C_{60} and 20 nm SnO_x deposited by ALD allowed for conformal coating (Figure S3, Supporting Information).

2.3. Implementation in Monolithic Perovskite Silicon Tandem Solar Cells

The optimized top cell absorber $\text{FA}_{0.75}\text{Cs}_{0.25}\text{Pb}(\text{I}_{0.8}\text{Br}_{0.2})_3$ with a 1.1 M precursor solution was implemented in monolithic perovskite silicon tandem solar cells, using the cell structure presented in Section 2.1. A stabilized efficiency of 25.1% was certified by Fraunhofer ISE CalLab PV Cells (Figure 4). An efficiency histogram of all 12 tandem cells processed is presented in Figure S4, Supporting Information.

The highest certified result was obtained around 5 months after processing of the respective tandem batch. Within this time, we measured the cell regularly inhouse and at ISE CalLab PV Cells (photovoltaic parameters shown in Table S2, Supporting Information) and observed an increase in efficiency rather than degradation (all measurements in air, without encapsulation). Figure 5 shows the performance evolution over time for the certified tandem device. Inhouse measurements were carried out with a light-emitting diode (LED) sun simulator calibrated with a silicon solar cell. Here, also stabilized efficiency

measurements (fixed maximum power point voltage V_{MPP} from I - V scan tracked over time) were recorded and reveal a stable behavior under working conditions as shown in Figure 5b with slight efficiency increase over time.

EQE analysis (ISE Callab PV Cells) and reflection measurements of the tandem device are shown in Figure 6. Repetition of both measurements after 5 months gave similar results for the perovskite's EQE and device reflection; however, the silicon's EQE increased by around 9% corresponding to a rise in integrated J_{SC} of around 1.6 mA cm^{-2} . Moreover, a measurement artifact was present, but could be corrected according to Meusel et al.^[31] (Figure S5, Supporting information).

This EQE increase over a broad wavelength range suggests that it is not caused by an improvement of the collection probability of the heterojunction bottom cell, but rather by increased absorption due to reduced parasitic absorption in the overlying layers. Based on the current literature on single-junction perovskite solar cells,^[32] one hypothesis is that absorbing subbandgap states of the perovskite or its interfaces reduce the silicon current in the first place. These may disappear with storage time and lead to improved transmission to the silicon bottom cell. Consequently, the current mismatch of the two subcells is increased, which can explain the increase in FF (Table S2, Supporting Information).^[14,21] The reason for reduced hysteresis, slight increase in V_{OC} , and significant performance improvement might be connected with the mentioned vanishing of subbandgap states and lattice strain relaxation.^[32] Especially for monolithic tandem solar cells, such device changes are of utmost importance as operation close to current matching needs to be considered for highest performance. Thus, more investigation on the origin of device changes and long-term stability is required.

2.4. Next Steps Toward 30% Efficiency

In comparison with our previously published n-i-p monolithic perovskite silicon tandem devices using the same absorber

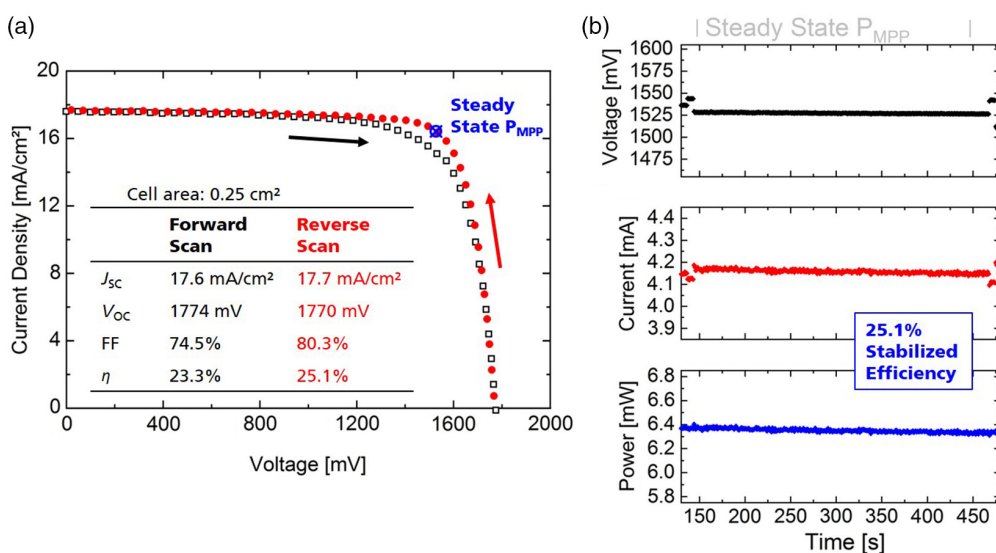


Figure 4. Certified tandem solar cell results from Fraunhofer ISE CalLab PV Cells of the best perovskite silicon tandem solar cell. a) J - V curve and corresponding photovoltaic parameters (inset). b) Steady-state tracking over time reaching 25.1% certified efficiency.

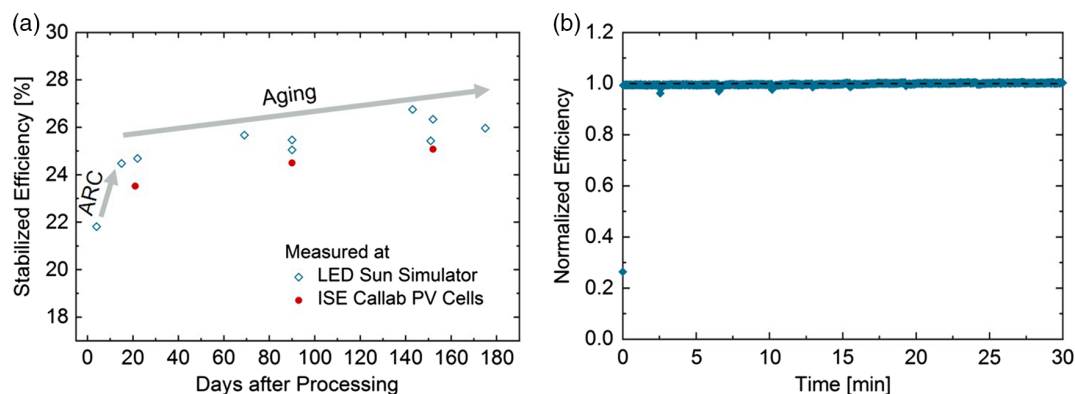


Figure 5. a) Evolution of stabilized efficiency values for different measurement days within 6 months after processing with an efficiency increase after application of 100 nm MgF₂ as ARC, followed by further efficiency increase over time (aging, tandem storage in the dark under N₂). Measurements were recorded at a spectrally noncalibrated LED sun simulator (blue) and with a calibrated spectrum at Fraunhofer ISE CalLab PV Cells (red) b) A representative stabilized efficiency measurement (normalized, corresponding to best performance obtained with the LED sun simulator ≈5 months after processing) over 30 min at V_{MPP} shows stable efficiency under working conditions. The dashed line shows the average efficiency (start at 30 s).

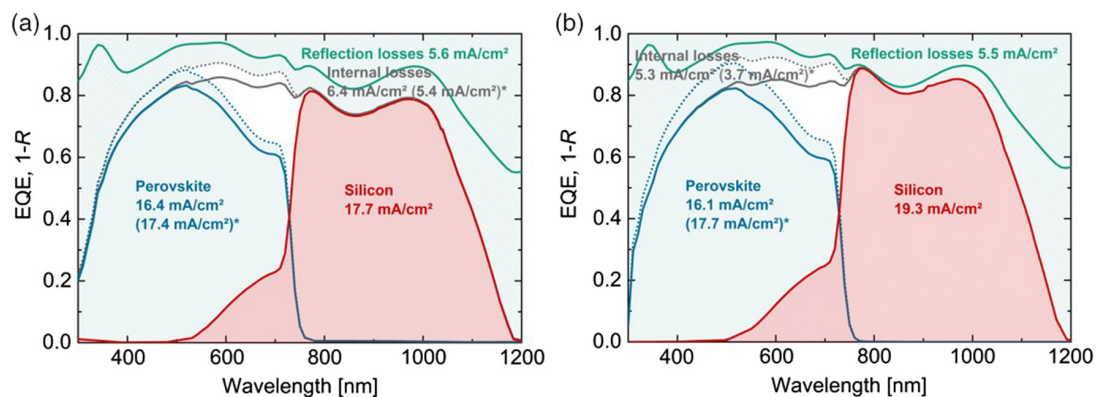


Figure 6. EQE of the perovskite top solar cell (blue) and the silicon bottom solar cell (red) measured at Fraunhofer ISE CalLab PV Cells and 1-Reflectance (R) of the tandem solar cell. The perovskite's EQE (solid line) is scaled to the photocurrent of the respective J–V curve (dashed line, marked with *). a) First measurement ≈1 month after processing and b) repeated measurement ≈5 months after processing; here a measurement artifact was removed according to Meusel et al.^[31] (see Figure S5, Supporting Information). Comparison of the two data sets shows similar perovskite EQE and reflection, however increased silicon EQE and reduced internal losses in the measurement after 5 months.

composition,^[21] the change in device polarity to p–i–n allows for an improved FF and J_{SC}. This is due to the favorable optics and the thin charge transport materials that are used in the p–i–n device architecture. However, the V_{OC} decreased by around 70 mV when switching from n–i–p to p–i–n, even though the p-type bottom cell (≈730 mV) provides a slightly higher V_{OC} compared with the n-type bottom cell (≈720 mV). To clarify the origin of this drop, we determined the internal quasi-Fermi-level splitting (QFLS) from absolute photoluminescence (PL) measurements (Figure 7).^[33,34] Layer stacks of the perovskite in combination with the different transport layers were examined.

Here, the limiting interface of the high bandgap perovskite was found to be the perovskite/electron transport layer (ETL) interface. Addition of the ETL resulted in a drop of the QFLS of 36 meV compared with the hole transport layer (HTL)/perovskite layer stack. We assume that the evaporation of C₆₀

at low rates does not damage the perovskite and, thus, attribute the drop in QFLS to increased nonradiative recombination at the perovskite/ETL interface as previously observed for other perovskite compositions.^[33,35] To overcome this limitation, a series of passivation layers were added between the perovskite/ETL interface, namely, evaporated LiF, poly(methyl methacrylate) (PMMA), and a blend of [6,6]-phenyl-C₆₁-butyric acid methyl ester (PCBM) and PMMA. Consistently with previous reports,^[21,25,36,37] these interlayers improved the photoluminescence quantum yield (PLQY) reducing the nonradiative recombination at the interface with C₆₀. The strongest effect was obtained with the PMMA interlayer, which induced a gain of 21 meV, pushing the QFLS to 1.189 eV. Noteworthy, reaching such a V_{OC} in the subcell of the tandem device would allow to increase efficiency up to 26.7%. On the contrary, the measured V_{OC} in the single-junction solar cell of 1.08 V lies well below the QFLS of the respective (unpassivated) HTL/perovskite/ETL stack

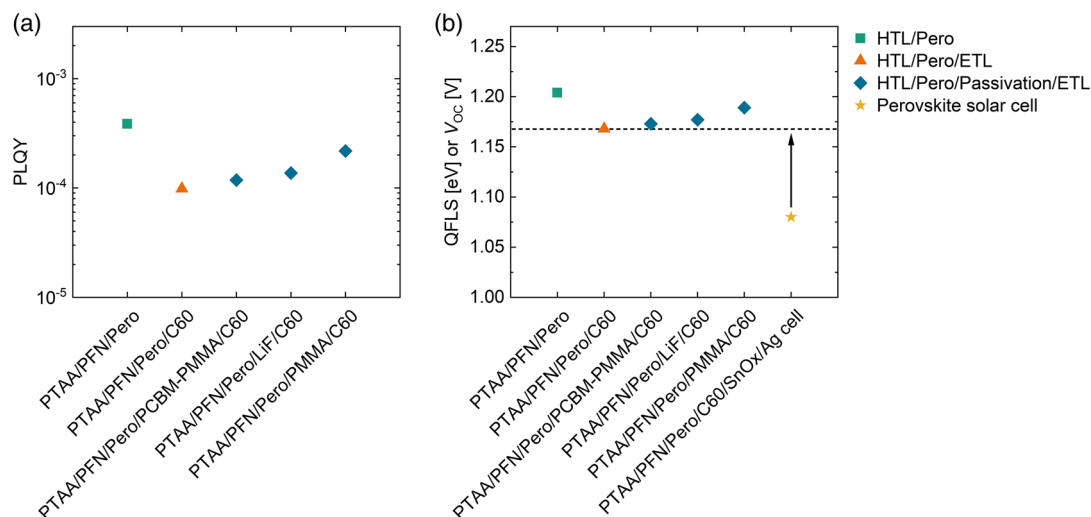


Figure 7. a) PL quantum yield measurements of the high bandgap perovskite (1.68 eV) in combination with its charge transport layers and additional passivation layers at the perovskite/C₆₀ interface. b) Deduced QFLS of each layer stack, as well as the V_{OC} from the respective single-junction device. The arrow highlights the offset between the V_{OC} of the solar cell and the QFLS of the respective p–i–n layer stack (dashed line).

(1.168 eV). This implies that the difference of the majority carrier quasi-Fermi levels at the respective contacts is actually lower than the QFLS within the volume of the perovskite absorber layer. Thus, in addition to nonradiative bulk and interfacial recombination, an unfavorable band alignment occurs at the interfaces, possibly due to injection/tunnel barriers^[33,38] and/or (ionic) charge accumulation at the interfaces. Thus, investigation on energetically adapted charge transport layers for the 1.68 eV perovskite and their passivation will be crucial to realize the full potential of the high bandgap perovskite absorber.

Furthermore, the tandem current needs to be improved. Our simple planar MgF₂ ARC still leaves 5.5 mA cm⁻² of current loss in the tandem device due to reflection (Figure 6). More advanced antireflection strategies, such as foils or additional polymer layers with pyramidal or moth-eye structuring, could further minimize reflection losses.^[11,18,39,40] In addition, our tandem devices so far feature a comparably thick ITO recombination layer between the two subcells that can give rise to significant reflection losses due to large changes in refractive indices comparing silicon to the transparent conductive oxide and perovskite.^[13] It can be replaced by a thinner ITO layer or exchanged by a tunnel diode for reduced reflection losses to increase the current in the silicon bottom cell.^[7,14,41,42] In a last step, simulation and spectral analysis can finally give valuable guidelines to fine-tune the perovskite absorber (thickness, bandgap) to reach a point close to current matching of the two subcells. A rise of tandem J_{SC} to 20 mA cm⁻² as already achieved,^[43,44] together with 1879 mV (QFLS with PMMA passivation), and the presented FF of 80% would enable 30% perovskite silicon tandem devices.

3. Conclusion

In this work, we presented a 25.1% certified efficiency for a monolithic perovskite silicon tandem solar cell with a MA-free high bandgap composition and FF reaching 80%. A variation

of the precursor's molarity effectively increased the absorber's layer thickness and current collection of perovskite solar cells. Improved absorption close to the band edge and excellent film quality with large crystal grains were obtained for 1.1 M FA_{0.75}Cs_{0.25}Pb(I_{0.8}Br_{0.2})₃ precursor solutions. An increase in molarity went along with changes in crystallization dynamics and stress-related film wrinkling. Adapted thickness of subsequent evaporation and ALD processes enabled conformal contact deposition on wrinkled perovskite and high device performance. Moreover, an efficiency improvement was observed for tandem devices over 5 months when stored under N₂ in the dark. Further long-term investigations under operating conditions need to be carried out to understand performance evolution and their causes. Furthermore, we presented a loss analysis of our top cell based on QFLS measurements, which highlighted the limitations imposed by the perovskite/C₆₀ interface on the V_{OC} of the top cell. Potential passivation layers such as LiF and PMMA show improved quasi-Fermi-level splitting. In addition, the comparatively high reflection losses of 5.5 mA cm⁻² need to be reduced for further advancements, for instance, by using a moth-eye structured foil. Together, these measures make over 30% efficient monolithic perovskite silicon tandem solar cells a realistic target in the near future.

4. Experimental Section

Silicon Bottom Cell Fabrication: Silicon solar cells were fabricated from 250 μm-thick silicon wafers (Siltronic, p-type, float zone, base resistivity 1 Ω cm). A pyramidal texture was etched using potassium hydroxide (KOH) on one side of the wafer. After RCA cleaning the silicon surface, an intrinsic + doped amorphous silicon passivation layer stack was deposited on both sides using plasma-enhanced chemical vapor deposition (PECVD) in an Indeotec cluster tool. The thickness of the undoped layer was ≈6.0 nm on the planar and the textured side; the thickness is defined via the deposition time, which was longer for the textured side to account for the increased surface area compared with the planar side. The thickness of the n-doped and p-doped amorphous silicon layer was 12 nm.

The amorphous silicon deposition was performed in a parallel-plate PECVD reactor powered at 13.56 MHz, at 200 °C using mixtures of silane (SiH₄), hydrogen (H₂), phosphine (PH₃), and trimethylboron (TMB). Subsequently, ITO (In₂O₃/SnO₂ = 90/10 wt%) was DC sputtered in an Oxford Instruments cluster tool on both sides using mixtures of argon and oxygen. On the textured side 195 nm of ITO was deposited on the full area, on the planar side ≈80 nm of ITO was sputtered through a shadow mask with 6 mm × 6 mm openings defining the individual cells of the tandem device. Increased deposition time was applied for the textured side taking the higher surface area compared with the planar side into account. Before a-Si and ITO deposition, the wafers were dipped in an aqueous solution of 1% hydrogen fluoride (HF) to remove silicon oxide (SiO₂). After ITO sputtering, a 1000 nm-thick silver layer was deposited on the textured side of the wafer as a rear contact. Finally, the wafers were cut by a chop saw in 2.5 cm × 2.5 cm large substrates each containing four ITO pads.

Perovskite Top Cell Fabrication: Perovskite top solar cells were fabricated in the planar p–i–n architecture using low-temperature processes (≤100 °C). First, bottom cells were treated 15 min in a UV/Ozone Cleaner Plus from Bioforce Nanosciences. Then, 120 μL of 3 mg mL⁻¹ PTAA (Sigma-Aldrich) in toluene was spin coated at 6000 rpm for 30 s with an acceleration time of 3 s, followed by 10 min annealing at 100 °C. Then, 60 μL of 0.5 mg mL⁻¹ PFN-Br (1-Material) in methanol was spin-dropped at 5000 rpm for 20 s. For the perovskite absorber, stoichiometric weighing of formamidinium iodide (FAI, Greatcell Solar), caesium iodide (CsI, 99.999%, Sigma-Aldrich), lead bromide (PbBr₂, 99.999%, Sigma-Aldrich), and lead iodide (PbI₂, 99.99%, TCI) was carried out for FA_{0.75}Cs_{0.25}Pb(I_{0.8}Br_{0.2})₃. Dimethyl sulfoxide (DMSO, ≥99.9%, Sigma-Aldrich) and dimethyl formamide (DMF, 99.8%, Sigma-Aldrich) (1:4) were added to give the optimized molarity of 1.1 M. The solution was stirred at 60 °C overnight and spin coated (150 μL per substrate) at 4000 rpm for 35 s with an acceleration time of 3 s with drop of 300 μL ethyl acetate (antisolvent) 10 s after the start. After 1 h of annealing at 100 °C, 15 nm of C₆₀ (Solenne) was thermally evaporated at 10⁻⁵–10⁻⁶ mbar with rates of around 0.3 Å s⁻¹. Then, 20 nm of SnO_x were deposited by ALD at 80 °C (FlexAL system from Oxford Instruments). Tetrakis(dimethylamino) tin(IV) (TDMASn) and deionized water were used as the metal precursor and the oxygen precursor, respectively. Argon was applied as purge gas with a flow rate of 200 sccm. The dose and purge times were 0.3/10/0.2/10 s for TDMASn/purge/H₂O/purge. TDMASn was heated to 50 °C while deionized water was kept at room temperature. The ITO front contact (70 nm thick) was sputtered in the Oxford Instruments cluster tool at low power of 40 W at 50 °C with 30 sccm argon. A shadow mask with 6 mm × 6 mm large openings was used aligning the front contact to the recombination layer between the two subcells. Subsequently, ≈170 nm thick silver (Ag) electrodes were thermally evaporated (pressure ≈10⁻⁶ mbar, rate 1 nm s⁻¹) through a mask defining a U-shaped busbar (5 mm between opposite busbar sides) for each of the four ITO pads. Finally, 100 nm of magnesium fluoride (MgF₂) was thermally evaporated (pressure ≈10⁻⁶ mbar, rate 1 nm s⁻¹) as antireflection coating (ARC).

Perovskite Single-Junction Solar Cell Fabrication: Perovskite single-junction solar cells shown in Figure 2 were fabricated on commercial ITO-coated glass (AMG, 7 Ω sq⁻¹, 25 × 25 mm²). The substrates were cleaned in acetone (2×), isopropanol (2×), and deionized water 5 min each and exposed to UV irradiation for 15 min. Afterward, similar processing was conducted for PTAA and PFN-Br as described for the perovskite top cell processing. For the variation of the perovskite bandgap (fixed molarity of 1.0 M), stoichiometric weighing of formamidinium iodide, caesium iodide, lead bromide, and lead iodide was carried out for FA_{0.83}Cs_{0.17}Pb(I_{0.83}Br_{0.17})₃ and FA_{0.75}Cs_{0.25}Pb(I_{0.8}Br_{0.2})₃, respectively, and dimethyl sulfoxide and dimethyl formamide were added in a 1:4 volume ratio. For the molarity variation of FA_{0.75}Cs_{0.25}Pb(I_{0.8}Br_{0.2})₃ also 1.1 and 1.2 M precursor solutions were prepared. Perovskite spin coating, C₆₀ evaporation, and SnO_x ALD were kept similar to the top cell fabrication. Solar cells were finished by evaporation of 100 nm-thick Ag contacts. Sample stacks for PLQY measurements were processed similar to single-junction solar cells. The additional passivation layer of 1 nm LiF (Sigma-Aldrich) was thermally evaporated at 10⁻⁵–10⁻⁶ mbar; in the case

of PMMA (Sigma-Aldrich) and the blend of [6,6]-phenyl-C₆₁-butyric acid methyl ester (PCBM, Solenne) and PMMA, 80 μL were spin-dropped at 5000 rpm for 30 s, followed by 10 min of annealing at 100 °C. PMMA (1 mg mL⁻¹) and PMMA (1 mg mL⁻¹)-PCBM (3 mg mL⁻¹) in chlorobenzene were prepared according to Peng et al.^[36]

Current–Voltage Characterization: Current–voltage (*I*–*V*) characteristics of perovskite silicon tandem solar cells were measured using a LED sun simulator (Wavelabs, Sinus-220). The perovskite single-junction solar cells were measured with a sun simulator equipped with a xenon short arc lamp and a Keithley 2651 A source meter in a glove box under nitrogen; over-estimation of currents was adjusted by a correction factor derived from measurements in nitrogen and in air of selected cells. In all cases, light intensity was calibrated to 1 sun under the AM1.5g spectrum using a silicon reference cell. All solar cells were first measured in forward and reverse scan direction (–0.1 to 1.9 V for tandem solar cells, –0.1 to 1.2 V for perovskite single-junction solar cells) with a scan speed of 47 mV s⁻¹ and a voltage step of 20 mV. For stabilized measurements, a fixed voltage (mean value of the maximum power point voltages obtained from forward and reverse scan) was set and the current was tracked over time. A shadow mask was used to define an active area of 0.25 cm². All measurements (*I*–*V* scans and stabilized measurements) have been repeated several times for each solar cell and data with highest performance is shown in the graphs.

CalLab PV Cells Measurements: Spectral response measurements of perovskite silicon tandem solar cells were measured at a laser-based measurement setup.^[45] Two different selective bias-illuminations and required bias-voltages were used to resolve both subcells.^[46] Bias-settings were adjusted to minimize measurement artifacts.^[31,47,48] *I*–*V* characteristics of perovskite silicon tandem solar cells were measured at a dual-source sun simulator (Wacom, WXS-220SL2). The light intensity was calibrated with filtered reference cells, each matching to a subcell. Spectral settings of the sun simulator were retrieved based on the spectral response of the subcells and calculated according to a generalized mismatch correction [IEC 60904-7; Ed.3 2008] by Meusel et al.^[49]

For the efficiency certification, *I*–*V* scans were recorded in both directions (*V*_{OC} → *I*_{SC} and *I*_{SC} → *V*_{OC}) within approximately 1 min per *I*–*V* curve. Then the cell was set to the point of maximum power *P*_{mp}, which is adjusted by slight variation of the voltage. The current and voltage was logged for 5 min (steady-state measurement) and another *I*–*V* scan in both direction was repeated. A detailed description of the measurement uncertainties can be found in the literature.^[50]

Absolute PL Measurements: Excitation for the PL imaging measurements was performed with a 520 nm continuous wave laser (Insaneware) through an optical fiber into an integrating sphere. The intensity of the laser was adjusted to a 1 sun equivalent intensity by illuminating a 1 cm²-size perovskite solar cell under short-circuit and matching the current density to the *J*_{SC} under the sun simulator (e.g., ≈22.0 mA cm⁻² at 100 mW cm⁻², or 1.375 × 10²¹ photons m⁻² s⁻¹ for a 83–17 triple cation perovskite cell). A second optical fiber was used from the output of the integrating sphere to an Andor SR393i-B spectrometer equipped with a silicon charge-coupled device camera (DU420A-BR-DD, iDus). The system was calibrated by using a halogen lamp with known spectral irradiance, which was shone into to integrating sphere. A spectral correction factor was established to match the spectral output of the detector to the calibrated spectral irradiance of the lamp. The spectral photon density was obtained from the corrected detector signal (spectral irradiance) by division through the photon energy (*hf*), and the photon numbers of the excitation and emission were obtained from numerical integration using Matlab. In a last step, three fluorescent test samples with high specified PLQY (≈70%) supplied from Hamamatsu Photonics where measured where the specified value could be accurately reproduced within a small relative error of less than 5%.

Further Characterization: Scanning electron microscopy images were taken with a Schottky emission SEM (Zeiss, Auriga 60) at 5 kV. An in-lets and a secondary electron detector were used for top-view (45° tilt) and cross-sectional imaging. Prior to analysis, a thin platinum layer was sputtered on the cross section of cut samples to improve conductivity.

Spectral response curves of single-junction perovskite solar cells were acquired on a custom-made spectral response setup at PV-Lab, Neuchâtel

equipped with a xenon lamp, a grating monochromator and lock-in amplifiers, with chopped light at a frequency of 232 Hz, and a beam size of 2 mm².

Reflectance and transmittance measurements were carried out using a Lambda 950 spectrophotometer from Perkin Elmer equipped with an integrating sphere (250–1200 nm, step size of 2 nm). Reflectance measurements of tandem devices were recorded at a LOANA solar cell analysis system from pv-tools.

AFM was performed on a Bruker Dimension Edge in a tapping mode with a scan rate of 0.1 Hz and a resolution of 512 × 512 points.

Supporting Information

Supporting Information is available from the Wiley Online Library or from the author.

Acknowledgements

This work was partially funded by the German Federal Ministry for Economic Affairs and Energy under contract number 0324037A (PersiST) as well as a Fraunhofer LIGHTHOUSE PROJECT (MaNiTU). A.J.B. gratefully acknowledges scholarship support from the Deutsche Bundesstiftung Umwelt (DBU). P.C. acknowledges financial support by HyPerCells, a joint graduate school of Potsdam University, and the HZB. Ö.Ş.K. gratefully acknowledges scholarship support from the Dr. Ruth Heerdts Stiftung. The authors would like to thank K. Fischer, N. Garder, V. Kübler, D. Kurt, L. Stevens, K. Wienands, L. Zafoschnig, J. Zielonka, and K. Zimmermann for support with processes, measurements, and technical issues.

Conflict of Interest

The authors declare no conflict of interest.

Keywords

heterojunction silicon solar cells, interfaces, perovskite solar cells, tandem solar cells, thin films

Received: March 20, 2020

Revised: April 20, 2020

Published online: May 26, 2020

- [1] S. Rühle, *Sol. Energy* **2016**, *130*, 139.
- [2] A. Richter, M. Hermle, S. W. Glunz, *IEEE J. Photovolt.* **2013**, *3*, 1184.
- [3] M. Yamaguchi, K.-H. Lee, K. Araki, N. Kojima, *J. Phys. D: Appl. Phys.* **2018**, *51*, 133002.
- [4] T. Leijtens, K. A. Bush, R. Prasanna, M. D. McGehee, *Nat. Energy* **2018**, *25*, 668.
- [5] M. T. Hörantner, H. J. Snaith, *Energy Environ. Sci.* **2017**, *10*, 1983.
- [6] M. H. Futscher, B. Ehrler, *ACS Energy Lett.* **2016**, *1*, 863.
- [7] J. P. Mailoa, C. D. Bailie, E. C. Johlin, E. T. Hoke, A. J. Akey, W. H. Nguyen, M. D. McGehee, T. Buonassisi, *Appl. Phys. Lett.* **2015**, *106*, 121105.
- [8] K. A. Bush, A. F. Palmstrom, Z. J. Yu, M. Boccard, R. Cheacharoen, J. P. Mailoa, D. P. McMeekin, R. L. Z. Hoye, C. D. Bailie, T. Leijtens, I. M. Peters, M. C. Minichetti, N. Rolston, R. Prasanna, S. Sofia, D. Harwood, W. Ma, F. Moghadam, H. J. Snaith, T. Buonassisi, Z. C. Holman, S. F. Bent, M. D. McGehee, *Nat. Energy* **2017**, *2*, 17009.
- [9] F. Sahli, J. Werner, B. A. Kamino, M. Bräuninger, R. Monnard, B. Paviet-Salomon, L. Barraud, L. Ding, J. J. Diaz Leon, D. Sacchetto, G. Cattaneo, M. Despeisse, M. Boccard, S. Nicolay, Q. Jeangros, B. Niesen, C. Ballif, *Nat. Mater.* **2018**, *17*, 820.
- [10] G. Nogay, F. Sahli, J. Werner, R. Monnard, M. Boccard, M. Despeisse, F.-J. Haug, Q. Jeangros, A. Ingenito, C. Ballif, *ACS Energy Lett.* **2019**, *4*, 844.
- [11] M. Jošt, E. Köhnen, A. B. Morales-Vilches, B. Lipovšek, K. Jäger, B. Macco, A. Al-Ashouri, J. Krč, L. Korte, B. Rech, R. Schlattmann, M. Topič, B. Stannowski, S. Albrecht, *Energy Environ. Sci.* **2018**, *2*, 16196.
- [12] B. Chen, Z. Yu, K. Liu, X. Zheng, Y. Liu, J. Shi, D. Spronk, P. N. Rudd, Z. Holman, J. Huang, *Joule* **2019**, *3*, 177.
- [13] L. Mazzarella, Y.-H. Lin, S. Kirner, A. B. Morales-Vilches, L. Korte, S. Albrecht, E. Crossland, B. Stannowski, C. Case, H. J. Snaith, R. Schlattmann, *Adv. Energy Mater.* **2019**, *9*, 1803241.
- [14] E. Köhnen, M. Jošt, A. Morales Vilches, P. Tockhorn, A. Al-Ashouri, B. Macco, L. Kegelmann, L. Korte, B. Rech, R. Schlattmann, B. Stannowski, S. Albrecht, *Sustainable Energy Fuels* **2019**, *3*, 1995.
- [15] Oxford PV, *Oxford PV perovskite solar cell achieves 28% efficiency 2018*, <https://www.oxfordpv.com/news/oxford-pv-perovskite-solar-cell-achieves-28-efficiency> (accessed: March 2020).
- [16] Helmholtz Zentrum Berlin, *World Record: Efficiency of perovskite silicon tandem solar cell jumps to 29.15 per cent 2020*, [https://www.helmholtz-berlin.de/pubbin/news_seite?nid=21020;sprache=en;seitenid=\(accessed: March 2020\)](https://www.helmholtz-berlin.de/pubbin/news_seite?nid=21020;sprache=en;seitenid=(accessed: March 2020)).
- [17] R. Fan, N. Zhou, L. Zhang, R. Yang, Y. Meng, L. Li, T. Guo, Y. Chen, Z. Xu, G. Zheng, Y. Huang, L. Li, L. Qin, X. Qiu, Q. Chen, H. Zhou, *Sol. RRL* **2017**, *1*, 1700149.
- [18] K. A. Bush, S. Manzoor, K. Frohna, Z. J. Yu, J. A. Raiford, A. F. Palmstrom, H.-P. Wang, R. Prasanna, S. F. Bent, Z. C. Holman, M. D. McGehee, *ACS Energy Lett.* **2018**, *3*, 2173.
- [19] Z. Qiu, Z. Xu, N. Li, N. Zhou, Y. Chen, X. Wan, J. Liu, N. Li, X. Hao, P. Bi, Q. Chen, B. Cao, H. Zhou, *Nano Energy* **2018**, *53*, 798.
- [20] F. Hou, L. Yan, B. Shi, J. Chen, S. Zhu, Q. Ren, S. An, Z. Zhou, H. Ren, C. Wei, Q. Huang, G. Hou, X. Chen, Y. Li, Y. Ding, G. Wang, D. Zhang, Y. Zhao, X. Zhang, *ACS Appl. Energy Mater.* **2019**, *2*, 243.
- [21] A. J. Bett, P. S. C. Schulze, K. M. Winkler, Ö. S. Kabakli, I. Ketterer, L. E. Mundt, S. K. Reichmuth, G. Siefert, L. Cojocar, L. Tutsch, M. Bivour, M. Hermle, S. W. Glunz, J. C. Goldschmidt, *Prog. Photovolt.* **2019**, *28*, 99.
- [22] J. Xu, C. C. Boyd, Z. J. Yu, A. F. Palmstrom, D. J. Witter, B. W. Larson, R. M. France, J. Werner, S. P. Harvey, E. J. Wolf, W. Weigand, S. Manzoor, Maikel F. A. M. van Hest, J. J. Berry, J. M. Luther, Z. C. Holman, M. D. McGehee, *Science* **2020**, *367*, 1097.
- [23] A. Dualeh, P. Gao, S. I. Seok, M. K. Nazeeruddin, M. Grätzel, *Chem. Mater.* **2014**, *26*, 6160.
- [24] K. A. Bush, K. Frohna, R. Prasanna, R. E. Beal, T. Leijtens, S. A. Swifter, M. D. McGehee, *ACS Energy Lett.* **2018**, *3*, 428.
- [25] M. Stolterfoht, C. M. Wolff, J. A. Márquez, S. Zhang, C. J. Hages, D. Rothhardt, S. Albrecht, P. L. Burn, P. Meredith, T. Unold, D. Neher, *Nat. Energy* **2018**, *3*, 847.
- [26] R. Carron, C. Andres, E. Avancini, T. Feurer, S. Nishiwaki, S. Pisoni, F. Fu, M. Lingg, Y. E. Romanyuk, S. Buecheler, A. N. Tiwari, *Thin Solid Films* **2019**, *669*, 482.
- [27] U. Rau, B. Blank, T. C. M. Müller, T. Kirchartz, *Phys. Rev. Appl.* **2017**, *7*, 044016.
- [28] S. Braunger, L. E. Mundt, C. M. Wolff, M. Mews, C. Rehermann, M. Jošt, A. Tejada, D. Eisenhauer, C. Becker, J. A. Guerra, E. Unger, L. Korte, D. Neher, M. C. Schubert, B. Rech, S. Albrecht, *J. Phys. Chem.* **2018**, *122*, 17123.
- [29] J. Zhao, Y. Deng, H. Wei, X. Zheng, Z. Yu, Y. Shao, J. E. Shield, J. Huang, *Sci. Adv.* **2017**, *3*, ea05616.
- [30] K. A. Bush, N. Rolston, A. Gold-Parker, S. Manzoor, J. Hausele, Z. J. Yu, J. A. Raiford, R. Cheacharoen, Z. C. Holman,

- M. F. Toney, R. H. Dauskardt, M. D. McGehee, *ACS Energy Lett.* **2018**, 3, 1225.
- [31] M. Meusel, C. Baur, G. Létay, A. W. Bett, W. Warta, E. Fernandez, *Prog. Photovolt.* **2003**, 11, 499.
- [32] S. Moghadamzadeh, I. M. Hossain, M. Jakoby, B. Abdollahi Nejand, D. Rueda-Delgado, J. A. Schwenzler, S. Gharibzadeh, T. Abzieher, M. R. Khan, A. A. Haghighirad, I. A. Howard, B. S. Richards, U. Lemmer, U. W. Paetzold, *J. Mater. Chem. A* **2020**, 8, 670.
- [33] M. Stolterfoht, P. Caprioglio, C. M. Wolff, J. A. Márquez, J. Nordmann, S. Zhang, D. Rothhardt, U. Hörmann, Y. Amir, A. Redinger, L. Kegelman, F. Zu, S. Albrecht, N. Koch, T. Kirchartz, M. Saliba, T. Unold, D. Neher, *Energy Environ. Sci.* **2019**, 12, 2778.
- [34] P. Caprioglio, M. Stolterfoht, C. M. Wolff, T. Unold, B. Rech, S. Albrecht, D. Neher, *Adv. Energy Mater.* **2019**, 9, 1901631.
- [35] P. Caprioglio, F. Zu, C. M. Wolff, J. A. Márquez Prieto, M. Stolterfoht, P. Becker, N. Koch, T. Unold, B. Rech, S. Albrecht, D. Neher, *Sustainable Energy Fuels* **2019**, 3, 550.
- [36] J. Peng, Y. Wu, W. Ye, D. A. Jacobs, H. Shen, X. Fu, Y. Wan, T. Duong, N. Wu, C. Barugkin, H. T. Nguyen, D. Zhong, J. Li, T. Lu, Y. Liu, M. N. Lockrey, K. J. Weber, K. R. Catchpole, T. P. White, *Energy Environ. Sci.* **2017**, 10, 1792.
- [37] J. Peng, J. I. Khan, W. Liu, E. Ugur, T. Duong, Y. Wu, H. Shen, K. Wang, H. Dang, E. Aydin, X. Yang, Y. Wan, K. J. Weber, K. R. Catchpole, F. Laquai, S. de Wolf, T. P. White, *Adv. Energy Mater.* **2018**, 8, 1801208.
- [38] C. M. Wolff, P. Caprioglio, M. Stolterfoht, D. Neher, *Adv. Mater.* **2019**, 31, 1902762.
- [39] R. Brunner, O. Sandfuchs, C. Pacholski, C. Morhard, J. Spatz, *Laser Photonics Rev.* **2012**, 6, 641.
- [40] A. Gombert, B. Bläsi, in *Functional Properties of Bio-Inspired Surfaces: Characterization and Technological Applications* (Eds.: E. A. Favret, N. O. Fuentes), World Scientific, Singapore, London, New Jersey **2009**, p. 79.
- [41] B. A. Kamino, B. Paviet-Salomon, S.-J. Moon, N. Badel, J. Levrat, G. Christmann, A. Walter, A. Faes, L. Ding, J. J. Diaz Leon, A. Paracchino, M. Despeisse, C. Ballif, S. Nicolay, *ACS Appl. Energy Mater.* **2019**, 2, 3815.
- [42] F. Sahli, B. A. Kamino, J. Werner, M. Bräuninger, B. Paviet-Salomon, L. Barraud, R. Monnard, J. P. Seif, A. Tomasi, Q. Jeangros, A. Hessler-Wyser, S. de Wolf, M. Despeisse, S. Nicolay, B. Niesen, C. Ballif, *Adv. Energy Mater.* **2018**, 8, 1701609.
- [43] Oxford PV, *Oxford PV sets world record for perovskite solar cell 2018*, <https://www.oxfordpv.com/news/oxford-pv-sets-world-record-perovskite-solar-cell> (accessed: March 2020).
- [44] M. A. Green, Y. Hishikawa, E. D. Dunlop, D. H. Levi, J. Hohl-Ebinger, M. Yoshita, A. W. Y. Ho-Baillie, *Prog. Photovolt.* **2019**, 27, 3.
- [45] M. Mundus, D. Lill, J. Hohl-Ebinger, W. Warta, in *29th European Photovoltaic Solar Energy Conf. and Exhibition*, WIP Wirtschaft und Infrastruktur GmbH & Co., Munchen **2014**, p. 3439.
- [46] J. Burdick, T. Glatfelter, *Solar Cells* **1986**, 18, 301.
- [47] G. Siefer, C. Baur, A. W. Bett, in *Proc. of the 35th IEEE on Photovoltaic Specialist Conf.*, IEEE, Piscataway, NJ **2010**, p. 704.
- [48] M. A. Steiner, J. F. Geisz, T. E. Moriarty, R. M. France, W. E. McMahon, J. M. Olson, S. R. Kurtz, D. J. Friedman, *IEEE J. Photovolt.* **2013**, 3, 879.
- [49] M. Meusel, R. Adelhelm, F. Dimroth, A. W. Bett, W. Warta, *Prog. Photovolt.* **2002**, 10, 243.
- [50] S. K. Reichmuth, G. Siefer, M. Schachtner, M. Mühleis, J. Hohl-Ebinger, S. W. Glunz, in *46th IEEE Proc. on Photovoltaic Specialists Conf. (PVSC)*, IEEE, Piscataway, NJ **2019**.